The Effect of Oxygen Fugacity On The Speciation of Manganese In Magmatic Systems

Stephanie C. Vaughn

Professor James Brenan

University of Toronto

Abstract

Redox state is an important intensive parameter to magmatic systems. Developing new methods to estimate the oxygen fugacity (fO_2) of natural samples is of great interest. The partitioning of redox sensitive elements into magmatic phenocrysts is one way of constraining fO_2 (Carmichael, 1991). Manganese (Mn) could be applicable in this regard as it can exist in multiple ionization states. The mineral apatite ($Ca_5(PO_4)_3(F, Cl, OH)$) is ubiquitous in felsic igneous rocks and the Mn content of apatite may constitute a potential redox sensor. Mn^{2+} is expected to be a much more compatible substitute for calcium (Ca^{2+}) in apatite than Mn^{3+} due to both charge balance and goodness of fit. This behavior was inferred by Miles et al. (2014), in which the Mn content of apatite was found to decrease with increased whole-rock Fe^{3+}/ Fe^{2+} in the zoned Criffell pluton of southern Scotland. However, it is not clear whether other parameters may affect Mn partitioning besides fO_2. The effect of fO_2 on partitioning was evaluated experimentally at 1-atmosphere to the test forsterite/glass partitioning of Mn and at 1 GPa to test the apatite/glass partitioning. No significant change in partitioning was recorded over a range of fO_2 from 3 below FMQ to 8 above. These results suggest that there is no change in the speciation of Mn across this range of fO_2. The large increase in partitioning recorded across the Criffell Pluton is attributed to a change in the activity of manganese caused by variation in temperature and composition.

I. Introduction

The redox state of a magmatic system is an important intensive parameter with a broad range of applications. It is important to understanding sulphur speciation, constraining mantle source rocks, and ore deposit models among other things. Despite this importance there are few methods available to estimate the oxygen fugacity (fO_2) of felsic magmas. One existing method of estimating the oxygen fugacity of natural rock samples calibrates redox from the composition of coexisting magnetite and ilmenite (Ghiorso and Sack, 1991). This method is widely accepted and has been applied to many studies, including that by Carmichael (1991), to use redox signatures to identify magma source regions.

Another existing method to estimate fO_2 is by measuring the partitioning of redox-sensitive elements in magmatic phenocrysts. The compatibility of a species in a crystal lattice depends on both its size and radius, and both of these parameters are known to change with oxidation state. One example of this method depends on the discrepancy in zircon-melt partitioning of cerium (Ce) at 3+ and 4+ oxidation states. This relationship was expressed quantitatively as a function of temperature, water content, melt composition (as a function of melt polymerization), and most importantly, oxygen fugacity (Smythe and Brenan, 2015). Another redox sensitive element that has potential in this regard is vanadium (V), which can exist in 2+, 3+, 4+ and 5+ oxidation states, over a range of fO_2 applicable to the highest extremes known in the solar system (Mallman and O'Neill, 2009). The relationship between vanadium and fO_2 is not as well defined as that for Ce but both studies rely on the same principle of using partitioning as a proxy for redox.

Another possible application of this principle is the partitioning of manganese (Mn) into apatite crystals. The compatibility of manganese in the apatite crystal lattice, as a substitute for calcium (Ca^{2+}) is predicted to decrease at more oxidized states (Mn^{3+}) compared to that of a more reduced oxidation state (Mn^{2+}) based on both the goodness of fit (ionic radius) and charge balance. This behaviour was suggested in an empirical study of the zoned Criffell Pluton of Scotland, presented by Miles et al. (2014). The Criffell Pluton is a zoned granitic pluton that records more oxidized conditions in the outer zones (Zone 1) and more reduced conditions in the inner zones (Zone 4) as well as decrease in whole-rock Mn-content and an increase in Mn-

content of apatite from zones 1 to 4 (Miles et al., 2014). This effect can also be expressed as an increase in the apatite/whole-rock partition coefficient of manganese.

This observed trend is supported by thermochemical speciation models of pure oxide phases for manganese as well as a small number of empirical results presented in the paper. A constitutive equation to express oxygen fugacity, dependent solely on the concentration of Mn in apatite is proposed by Miles et al. (2014), and is presented below. Although the proposed equation fits this limited dataset considered in this study reasonably well, with an R^2 value of 0.88, further study is needed. There are numerous shortcomings of the model including the problems associated with using a concentration as opposed to a partition coefficient, the high variability between samples studies, and the fact that the thermochemical model upon which it is based does not factor in the change in activity of species dissolved in a melt or held within a crystal lattice.

$$\log fO_2 = -0.0022(\pm0.0003) * Mn(ppm) - 9.75(\pm0.46)$$

To constrain this model and directly evaluate the effect of redox state on the partitioning of manganese into apatite crystals, an experimental study is necessary. Changing only one parameter, fO_2, and keeping all other variables constant can evaluate partitioning directly as a function of redox conditions.

II. Theoretical background

Speciation of Manganese

Manganese, like iron, cerium and vanadium, is a redox sensitive element and can exist in multiple valence states. At more reduced conditions, manganese would be expected to exist predominantly in the divalent state (Mn^{2+}), and would shift towards higher oxidation states at more oxidizing conditions. This behaviour is expected at relatively oxidizing versus relatively reducing conditions, but the specific temperature and redox conditions at which these transitions occur is important to predict. The general redox equations governing these changes in speciation are presented below along with their associated equilibrium constants.

$$MnO + \frac{1}{4}O_2 = MnO_{3/4} \tag{1}$$

$$MnO_{3/4} + \frac{1}{4}O_2 = MnO_2 \tag{2}$$
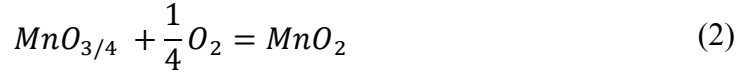
$$X_{Mn} = X_{Mn^{2+}} + X_{Mn^{3+}} + X_{Mn^{4+}} = 1 \tag{3}$$

$$K_1 = \frac{X_{MnO_{3/2}}}{X_{MnO} * fO_2^{1/4}} = \frac{X_{Mn^{3+}}}{X_{Mn^{2+}} * fO_2^{1/4}} \tag{4}$$

$$K_2 = \frac{X_{MnO_2}}{X_{MnO_{3/2}} * fO_2^{1/4}} = \frac{X_{Mn^{4+}}}{X_{Mn^{3+}} * fO_2^{1/4}} \tag{5}$$

Equation 1 represents the transition from Mn^{2+} to Mn^{3+}, governed by the equilibrium constant K_1 (equation 4), and equation 2 represents the transition from Mn^{3+} to Mn^{4+}, and is governed by the equilibrium constant K_2 (equation 5). Equation 3 is a statement of mass balance for manganese in the system. This system of equations can be solved to find the mole fraction of each species at a given fO_2 and a specified temperature.

The equilibrium constant (K_{eq}) is defined as $-RT \; lnK_{eq} = \Delta^o G_f$ where R is the gas constant and temperature (T) is in degrees kelvin. Speciation therefore has a temperature dependence. Using standard state chemical data for the Gibbs free energy of formation of species MnO, MnO_2 and Mn_2O_3 and creating a regression of the temperature data given, the free energy of formation of each species at any desired temperature can be estimated (Barin and Platzki, 1995). The entire set of calculations used to create the thermochemical model from the equations so far presented can be found in Box 1. The resulting thermochemical model, calculated at 1300°C, 1000°C, and 950°C, is presented in Figure 1 below.

It should be noted that Figure 1 is plotted as a function of the relative oxygen fugacity. The reaction curves for solid-state buffers exhibit the same temperature dependency, such that the deviation between two buffer curves is the same cross a range of temperature. As stated in equation 6, by subtracting the log fO_2 of a buffer at a specific temperature from the log fO_2 of a

sample at the same temperature, the resulting value is a measure of the relative oxygen fugacity (ΔFMQ). This allows the oxygen fugacity of multiple samples at different temperatures to be expressed on the same graph.

$$\Delta FMQ = \log f_{O_2}(sample\ (T_1)) - \log f_{O_2}(FMQ(T_1)) \qquad (6)$$
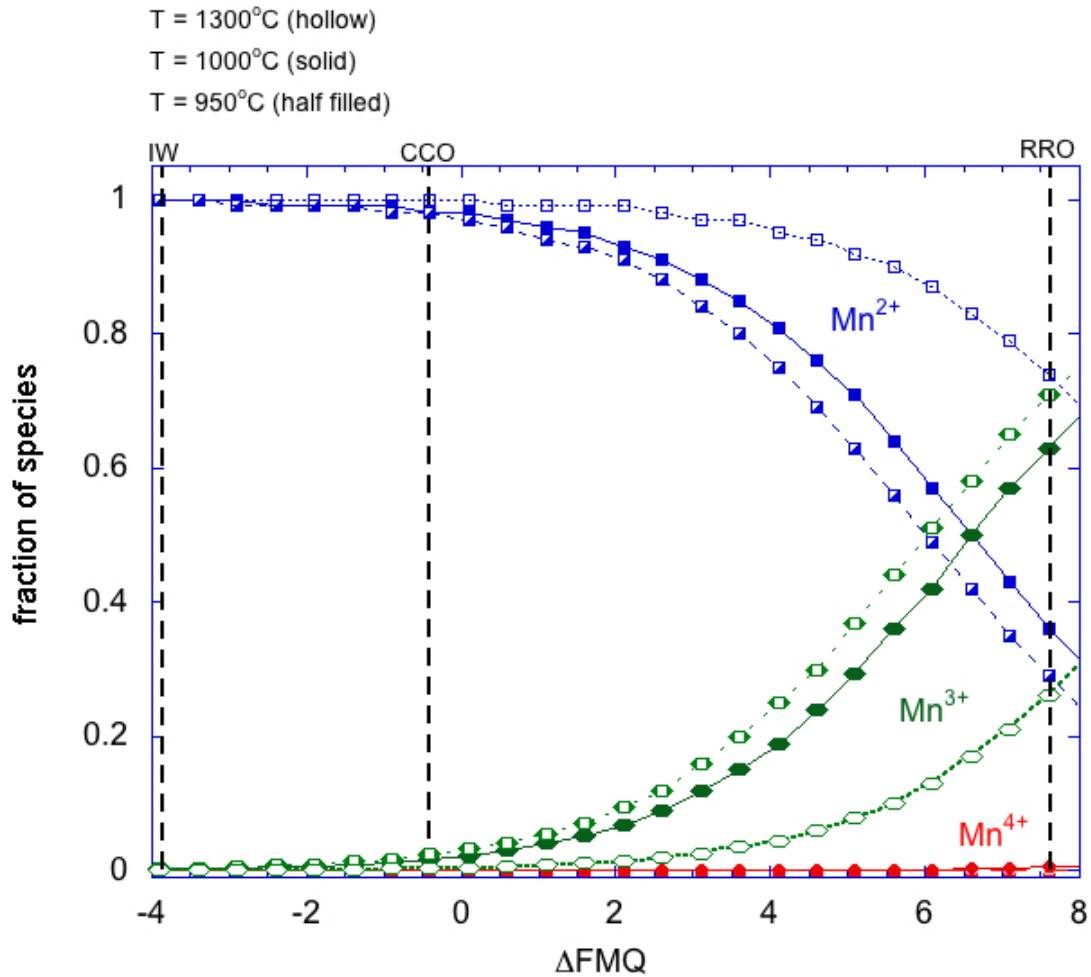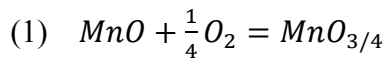

Figure 1: Thermochemical model of the speciation of Mn at various temperatures, plotted as the mole fraction of each species as a function of the relative oxygen fugacity

As predicted from the thermodynamic equations, and illustrated in Figure 1, speciation has a strong temperature dependence. At higher temperatures the crossover point where the theoretical distribution of Mn^{2+} and Mn^{3+} is equal shifts to more oxidizing conditions.

Box 1: Thermochemical calculations

(1) $MnO + \frac{1}{4}O_2 = MnO_{3/4}$ $\qquad K_1 = \dfrac{X_{MnO_{3/2}}}{X_{MnO}*fO_2^{1/4}} = \dfrac{X_{Mn^{3+}}}{X_{Mn^{2+}}*fO_2^{1/4}}$
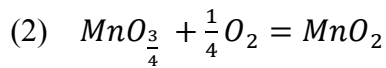
(2) $MnO_{\frac{3}{4}} + \frac{1}{4}O_2 = MnO_2$ $\qquad K_2 = \dfrac{X_{MnO_2}}{X_{MnO_{3/2}}*fO_2^{1/4}} = \dfrac{X_{Mn^{4+}}}{X_{Mn^{3+}}*fO_2^{1/4}}$

(3) $X_{Mn} = X_{Mn^{2+}} + X_{Mn^{3+}} + X_{Mn^{4+}} = 1$

$\longrightarrow \qquad X_{3+} = K_1 f_{O_2}^{1/4} * X_{2+}$

$$X_{3+} = K_1 f_{O_2}^{1/4} * (1 - X_{3+} - X_{4+})$$

$$X_{3+}\left(1 + K_1 f_{O_2}^{1/4}\right) = K_1 f_{O_2}^{1/4} * (1 - X_{4+})$$

$$X_{3+}\left(1 + K_1 f_{O_2}^{1/4}\right) = K_1 f_{O_2}^{1/4} * (1 - [K_1 f_{O_2}^{1/4} * X_{3+}])$$

$$X_{3+} + (X_{3+} * K_1 f_{O_2}^{1/4}) + (X_{3+} * K_1 K_2 * f_{O_2}^{1/4} * f_{O_2}^{1/4}) = K_1 f_{O_2}^{1/4}$$

$$X_{3+} = \frac{K_1 f_{O_2}^{1/4}}{1 + (K_1 f_{O_2}^{1/4}) + (K_1 K_2 f_{O_2}^{1/2})}$$

$\longrightarrow \qquad X_{4+} = K_2 f_{O_2}^{1/4} * X_{3+}$

$\longrightarrow \qquad X_{2+} = \dfrac{X_{3+}}{K_1 f_{O_2}^{1/4}}$

The temperatures used for this model approximate those of natural apatite crystallization temperatures and the melting point of intermediate magmas. Across a range of fO_2 from iron-wüstite (IW) (ΔFMQ= -4) to ruthenium-ruthenium oxide (RRO) (ΔFMQ=8) buffers, it is predicted that Mn^{4+} will not be present in the melt in significant amounts.

Although this model is helpful to our understanding of manganese speciation and how temperature and oxygen fugacity affect speciation, it is not directly applicable to a natural, or even an experimental, magma. The model is made for pure phases and assumes an activity coefficient of 1.0, such that the activity of a species in a melt is equal to its concentration. This assumes ideal behaviour for these species. Because manganese exists as a dissolved species in the melt, the activity coefficient of Mn is expected to deviate from 1 in a natural system. The equation relating activity (a_i) to concentration (X_i) using an activity coefficient (γ_i) is given by:

$$a_i = X_i\,\gamma_i$$

The reduced activity of manganese in a melt cannot be accurately measured or predicted. The only way to evaluate the change in speciation of manganese in a magmatic system is by measuring it. This can be done through direct methods, such as spectroscopy, or alternatively by monitoring the partitioning of manganese. Both a change in redox state and a change in activity can results in a change in partitioning. Using an experimental design in which composition, pressure and temperature are held constant for all experiments, fO_2 is the only variable tested. In this way, the activity of manganese is constant for all experiments so any measured change in partitioning would result directly from a change in the compatibility of manganese in apatite resulting from a change in speciation.

Apatite Structure and Mechanisms of Mn Substitution

It is expected that at reducing conditions, where Mn^{3+} is the dominant species of manganese in the melt, manganese would be significantly less compatible as a substitute for Ca^{2+} in apatite than at oxidizing conditions, when Mn^{2+} is the dominant species. This behaviour is expected because of both charge balance as well as the goodness of fit implied from the relative ionic radii of these species. Divalent calcium in 6-fold coordination has an effective ionic radius

of 1.14 Å while Mn^{2+} in 6-fold coordination in a high spin state has an effective ionic radius of 0.97 Å. In the same coordination and high spin state Mn^{3+} has an effective ionic radius of 0.785 Å (Elliott, 1994).

Apatite is a heavily studied mineral and is capable of making many complex substitutions. Apatite has a simplified chemical equation of $Ca_5(PO_4)_3(F,Cl,OH)$. There are two calcium cation sites, into which manganese might substitute, Ca(1), with a coordination number of 9, and Ca(2), with a coordination number of 7. Many cations may substitute into these sites, including rare earth elements (REE) with a 3+ charge. This substitution is favourable, specifically for europium (Eu) because the ionic radius of Eu^{3+} (1.09 Å) is very similar to that of calcium. For cations that do not have a 2+ charge to substitute into a calcium site, charge compensation becomes the important mechanism influencing the distribution between the two calcium sites. (Elliott, 1994) Both charge balance and goodness of fit are important to how favourable a substitution is, but apatite is able to make many different substitutions.

The most common substitutions that manganese makes in apatite crystals are as Mn^{2+} substituting for calcium or Mn^{5+} substituting for phosphorus as MnO_4^{3-}. Divalent manganese can most readily occupy the 9-coordinated Ca(1) site, the same site into which Fe^{2+} and Mg^{2+} are most likely to substitute. Mn^{2+} can occupy both calcium sites, but there is a preference for the Ca(1) site. Only at high Mn/Ca concentrations in the crystal will the Ca(2) site become commonly occupied. The preference for the Ca(1) site is attributed to the fact that the Ca(2) site is too large for manganese and this effect would be expected to be magnified in crystals with increased lattice parameters (Suitch, 1985). Divalent manganese has a larger ionic radius than trivalent manganese, so the limited compatibility into the Ca(2) site on the basis of size suggests even lower compatibility of Mn^{3+}.

Substitution of trivalent manganese in either calcium site is not mentioned in the literature, though there is a long record of other trivalent ions substituting for calcium in apatite, specifically REE. In these instances, charge balance is accomplished by substituting a monovalent cation for the other calcium (e.g. Li^+, Na^+, etc.), or by substituting a divalent anion, such as O^{2-} or S^{2-}. REE are commonly substituted into apatite because they have radii

comparable to Ca^{2+} and are readily accepted in the apatite lattice (Elliot, 1994). However, trivalent manganese has a radius that is over 30% smaller than that of Ca^{2+}.

It has also been noted that magnesium (Mg^{2+}) with an ionic radius of 0.86 Å is at or near the lower limit of the accepted size that is accepted into the apatite lattice. This suggests that Mg^{3+}, with a radius smaller than magnesium and the additional complication of charge balance, would not be an energetically favourable substitution into the apatite crystal.

On the basis of both size and charge balance, divalent manganese is much more compatible in an apatite crystal lattice than trivalent manganese. This is expected to manifest as a decrease in the apatite/melt partitioning of manganese at redox conditions where the mole fraction of Mn^{3+} exceeds that of Mn^{2+}. Referring back to Figure 1, it would be expected that, for example at 1000 ℃, the partition coefficient at IW or CCO buffers would be much greater than that at RRO buffer.

III. Experimental Methods

Part 1. Olivine-melt partitioning (1-Atmosphere)

The first set of experiments was completed to evaluate if there is any effect of fO_2 on the partitioning of manganese into olivine crystals. Three synthetic starting compositions were selected from a study of the partitioning of manganese between forsterite and silicate liquid (Watson, 1977). These compositions are plotted on the ternary forsterite-albite-anorthite in Figure 2, and the composition of each is shown in Table 1.

The starting compositions were oxide-mixes made using the following procedure. The appropriate weight of each oxide was measured out on a high accuracy bench scale. Calcium was added as $CaCO_3$ and sodium was added as Na_2CO_3. The appropriate concentration of CaO and Na_2O was therefore converted to these substances. All weighed components were ground in a mortar and pestle under ethanol. After the ethanol evaporated, the mix was calcined at 900 ℃ in air to remove the CO_2 from the system. The starting material was then fused in a platinum (Pt) crucible at 1300℃ for one hour in a Deltech drop-down furnace, and quenched to a glass in
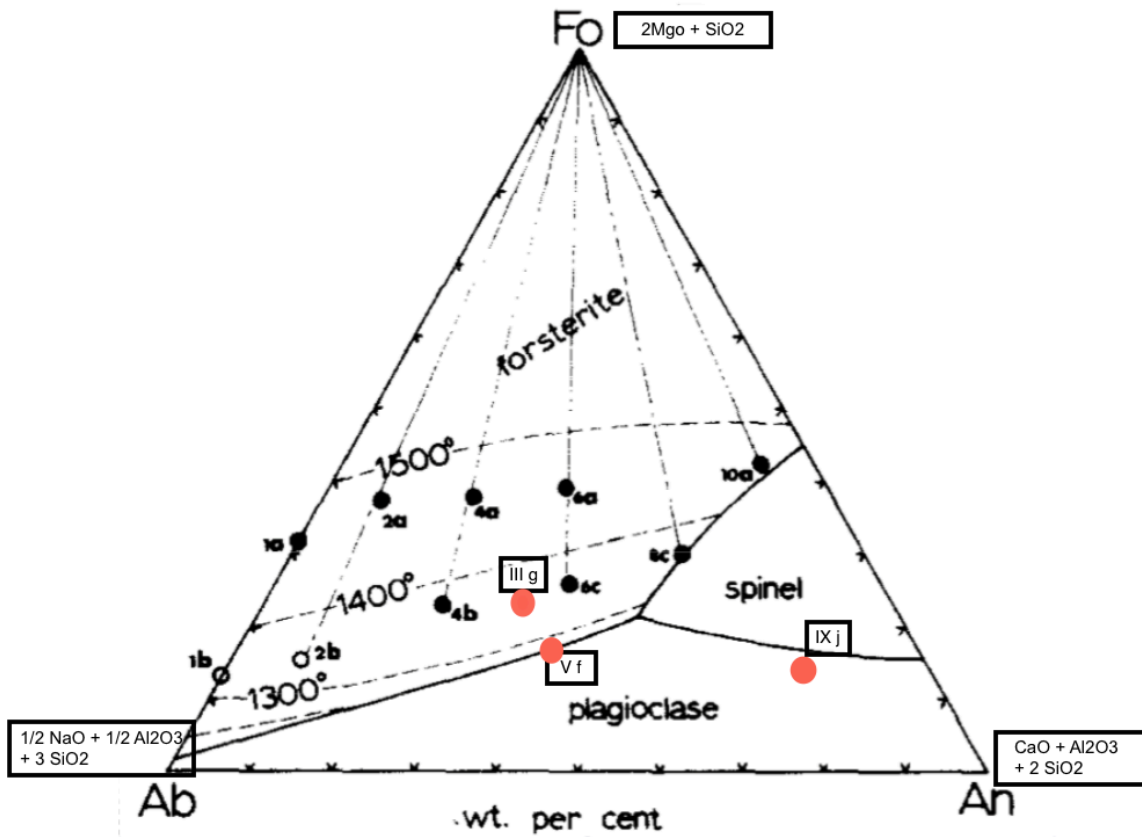
Figure 2: The three compositions selected for this study, plotted on a ternary diagram of the system Albite (Ab)-Anorththite (An)- Forsterite (Fo) (Miles, 1977)

	III g	V f	IX j
SiO2	63.2	56.5	47.2
Al2O3	20.1	19.2	21.5
MgO	8.8	10.8	13.8
CaO	4.4	8.0	15.2
Na2O	4.0	5.9	1.9
MnO	0.052	0.032	0.26
TOTAL=	100.6	100.4	99.9

Table 1: Weight percent oxides of the three starting compositions used in these experiments, taken from Miles, 1977

water. The sample was then removed from the crucible and ground to a powder. It was then fused, quenched and ground again to ensure a homogenous glass starting composition.

Some samples were doped with the trace elements: scandium (Sc), terbium (Tb), ytterbium (Yb), samarium (Sm), hafnium (Hf) and thorium (Th). Each element was added in the concentration of 50 ppm, as an acid solution with the concentration of 1000 $\frac{\mu g}{ml}$, with the exception of Hf with an original concentration of 10,000 $\frac{\mu g}{ml}$ that was diluted and then added using a syringe with 0.2 μl precision. This was done to monitor any auxiliary changes in partitioning of trace elements with fO_2.

Experiments were run in 1-atmosphere gas-mixing furnaces under a pre-calibrated mix of CO and CO_2 gasses to impose an fO_2. Samples were run with two different sample-holding assemblies. For the first, samples were loaded into Pt capsules that were welded on the bottom and open at the top and then held in an apparatus as illustrated in Figure 3a. Alternatively, the sample was loaded onto a Pt wire loop by suspending them using a polyvinyl alcohol (PVA) glue solution. Once the loops entered the furnace the PVA would evaporate and the samples would be held on the loop by surface tension. This is illustrated in Figure 3b. Both sample holders were suspended on a hook at the bottom of a length of silica glass.
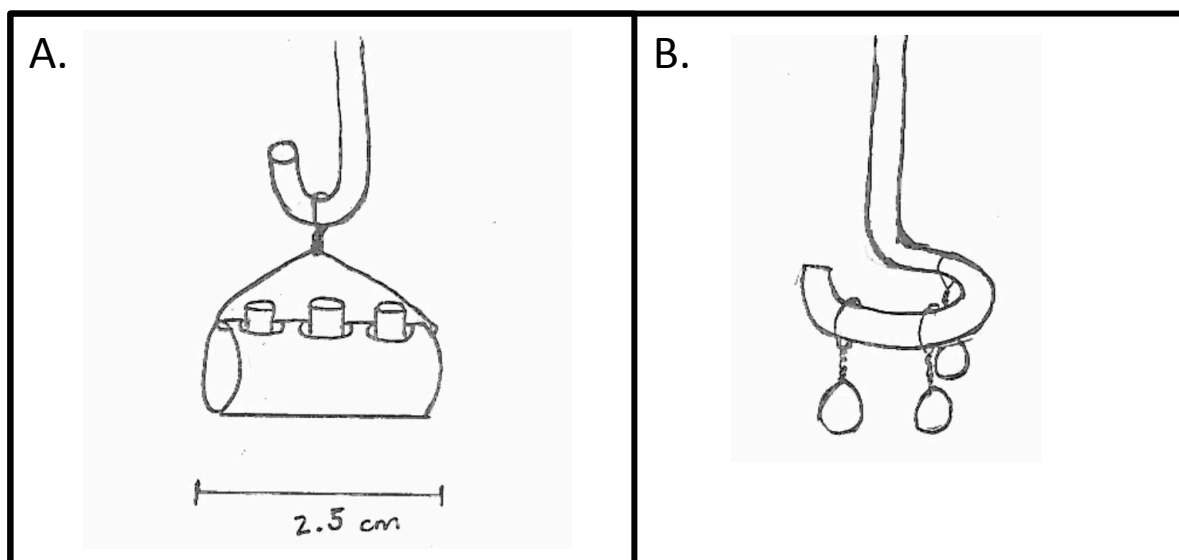

Figure 3: Schematic drawing of the sample holders used in the 1-atmosphere experiments. Figure 3a to the left shows the open Pt-capsules. Figure 3b to the right shows the samples suspended on a Pt wire loop. Both show how they attach onto the loop or hook to load them into the hotspot of the furnace.

Prior to running each experiment, a thermocouple and sensor to measure fO_2 was put inside the furnace at the desired gas flow, and temperature and fO_2 were measured after the system had time to equilibrate—at least 45 minutes. The sensor was then removed and the cap that held the sample was put in the furnace tube and sealed. The furnace then re-equilibrated to the desired fO_2 for 15-30 minutes (longer for more reduced conditions) before the sample was lowered into the hotspot of the furnace. At that point, the temperature program was started and the experiment was monitored until completion.

Three different heating programs were used for the experiments. Program 1 was a constant ramp from 1325°C to 1285°C at a constant rate of 2°C per hour. Program 2 consisted of a hold at 1325°C for 3 hours followed by a ramp to 1300°C at a rate of 90°C per hour, and finally a ramp to 1285°C at 2°C per hour followed by a hold until the end of the experiment. Program 3 was a hold at constant temperature, 1300 °C, for the duration, either 48 or 96 hours. At the completion of the run, samples were quickly lowered from the hotspot and quenched in air.

The specifications regarding the fO_2, composition, heating program and sample holding method used for each experiment is presented in Box 2 with the results of this set of experiments. Following each run, the run-products were mounted in epoxy and polished to the sample volume using 240 grit silicon carbide (SiC), followed by 600 grit SiC, then 1-micron and 0.3-micron Al_2O_3.

Part 2. Apatite-melt partitioning (Piston Cylinder)

This set of experiments, intended to measure the partitioning of manganese between crystals of apatite and an intermediate magma were conducted in the piston cylinder. A natural dacite starting material from Santorini, Greece, with a composition listed in Table 2, was doped with 1 weight% (wt%) manganese and between 2 and 8 wt% Durango apatite. It was then calcined, fused in a Pt crucible at 1300°C in the dropdown furnace and quenched in water.

Component	SiO_2	TiO_2	Al_2O_3	FeO	MgO	CaO	Na_2O	MnO	K_2O	P_2O_5	Total
Weight %	65.5	0.78	17.37	5.8	1.46	3.99	2.33	0.15	1.98	0.25	99.65

Table 2: Composition of Santorini dacite, prior to doping with manganese and phosphorus

The first three piston cylinder experiments were run hydrous in graphite-lined nickel capsules machined from a solid nickel rod. A pressure weld kept the water in the system once the stack was pressurized. This type of capsule was abandoned thereafter. The rest of the experiments were run in gold (Au) or platinum (Pt) capsules made of 1.5 cm lengths of 2 mm diameter tubing and welded on either end. Some runs also included an inner capsule of graphite or a silver-palladium (Ag-Pd) lining.

In these experiments redox was imposed in one of three ways. In some, solid-state "sandwich" buffers consisting of 50/50 mixes of each buffer component, for example, ruthenium metal and ruthenium oxide, were included on either end of the capsule. Another method to impose redox was to pre-equilibrate the starting material to a desired fO_2, for these experiments to the iron-wüstite (IW) buffer, at 900 °C for 10 or more hours. In this instance, iridium (Ir) powder was included in the capsule as a redox sensor. The last method used an inner graphite capsule to impose the carbon-carbon monoxide (CCO) buffer on the system, and included Ir as a redox sensor as well.

Because these experiments were done under hydrous conditions, and given the small amount of water in the system, care was taken to ensure that the water did not leave the system prior to, during or after the capsule was sealed. All the components to be included in a capsule were pre-weighed before loading began to speed the process and to compute how much water should be added to achieve 10 wt%. Water was loaded first, followed by iridium or a solid state buffer. The sample was loaded next and then the solid state buffer again on top (if being used). If a graphite inner capsule is being used, this procedure is followed to load the inner capsule and then placed inside the outer capsule last. After the capsules were loaded, the top was cleaned with a wipe to prevent any dust from getting in the weld and the top weld was completed on the arc welder. To keep the sample cool during welding, it was wrapped in a copper coil connected on the other end to the vice and placed in a water bath. It should be noted that the capsule is measured after every addition of new material both before and after the weld. The capsule is then put in the drying oven for an hour and again weighed to ensure that no water was lost from the system.

Once the capsules were prepared they were put in the assembly illustrated in Figure 4. MgO powder was packed between the capsules and the MgO part. This was done to protect the

capsules from puncture or from differential compaction, causing the loss of water from the system. As illustrated, the MgO parts are then put inside a graphite furnace, inside a pyrex sleeve and the graphite plug is put snuggly inside the pyrex sleeve. Three previously fabricated sodium chloride (NaCl) salt cells are then put around the pyrex sleeve. The whole thing is wrapped in lead foil and put inside the pressure vessel. A base plug goes on top of the assembly, inside to pressure vessel and a copper ring goes below. The pressure vessel is then put on the stack and the standard procedure to put the thermocouple in and to set up the piston cylinder stack is followed.

The stack is then pressurized to an end load of 3600 psi and the power leads and cooling water hoses are connected. The sample load is pressurized to 3650 psi (250 bar), corresponding to 1 GPa pressure on the sample. The same heating program was used for all of these experiments and only varied in the final temperature at which the experiment dwelled.
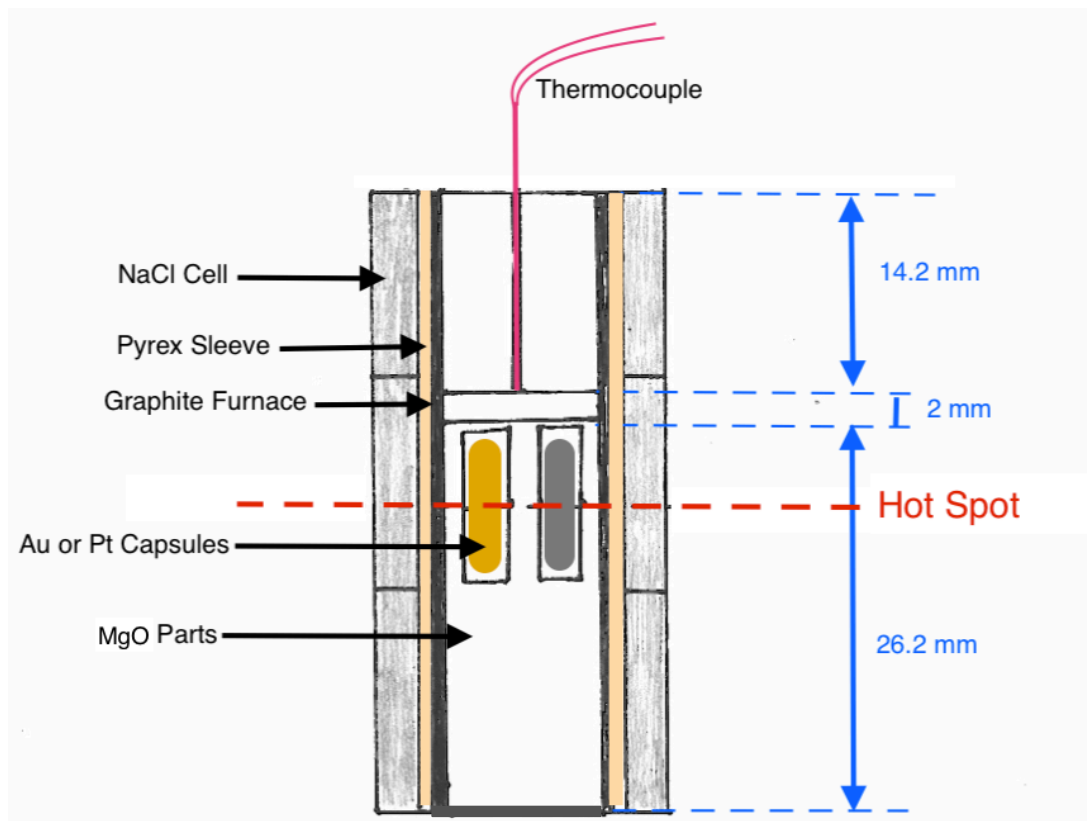

Figure 4: Piston cylinder sample assembly. Note that the thermocouple is illustrated here, but it is emplaced after the assembly is put into the pressure vessel and loaded onto the stack.

Figure 5: An experiment running in the piston cylinder. The two black cables are power leads and the silver disk in between is the pressure vessel, where the sample is located.

The heating program consisted of a ramp to temperature at a rate of 50°C per minute to the desired temperature, followed by a dwell time of 48 or 96 hours and then a step to zero degrees. For the first hour after the program is started the sample constantly loses pressure as the assembly compacts. The sample-load was monitored closely (every hour) for the first few hours

and then every 5-8 hours for the remainder of the experiment. Samples were quenched by terminating power, and the continued circulation of cooling water facilitated rapid cooling.

Following the completion of each experiment, the run-products were removed from the assembly and mounted individually in epoxy. After the epoxy set, the plugs and were polished into the sample volume using 240 grit SiC, 600 grit SiC, then 1-micron and 0.3-micron Al_2O_3. The specific conditions for each experiment are described in the results section of the report in Box 3.

IV. Analytical methods

Preliminary analysis of each sample was conducted on the scanning electron microscope (SEM). Prior to analysis, the polished plugs were carbon-coated to achieve a conductive surface necessary to use this analytical tool. The SEM was used to gather preliminary semi-quantitative compositional measurements, but also to decide if the sample was successful and if it qualified for further analysis on more accurate analytical tools. One such criteria that samples were evaluated for was to see if the desired phase (forsterite or apatite) was grown from the melt and if these crystals were of significant enough size (at least 5 microns in diameter, but ideally 10 microns or larger) for further analysis on the electron probe or LA-ICP-MS. The other major criteria for further analysis were that the run-products had quenched to a homogeneous glass without any crystallization of accessory phases.

If a sample was successful in these regards, it was selected for further analysis. Successful one-atmosphere samples were analyzed further on the laser ablation-inductively coupled plasma-mass spectrometer (LA-ICP-MS). Data reduction for LA-ICP-MS data was completed on the Matlab software SILLS.

Successful piston cylinder run-products were analyzed on the electron probe micro analyzer (EPMA). Ten or more analyses were performed each on the glass, apatite and iridium phases of each successful sample. The probe needs to be calibrated separately for each phase so each phase was measured separately.

V. Results

Part 1. Olivine-melt partitioning (1-Atmosphere)

Two of the three compositions selected were successful in growing olivine crystals. These two compositions were V f and IX j. Of these two compositions, IX j was more successful in growing olivine crystals of significant size and abundance. Temperature program 1 was the most successful temperature program in the same regard.

From the analyses of olivine and glass compositions done on the LA-ICP-MS, we were able to calculate olivine/melt partition coefficients for manganese. These values are shown as a function of the relative oxygen fugacity in Figure 6, below. The error associated with each value is quite large. This is a result of limited analyses and the small diameter of the olivine crystals
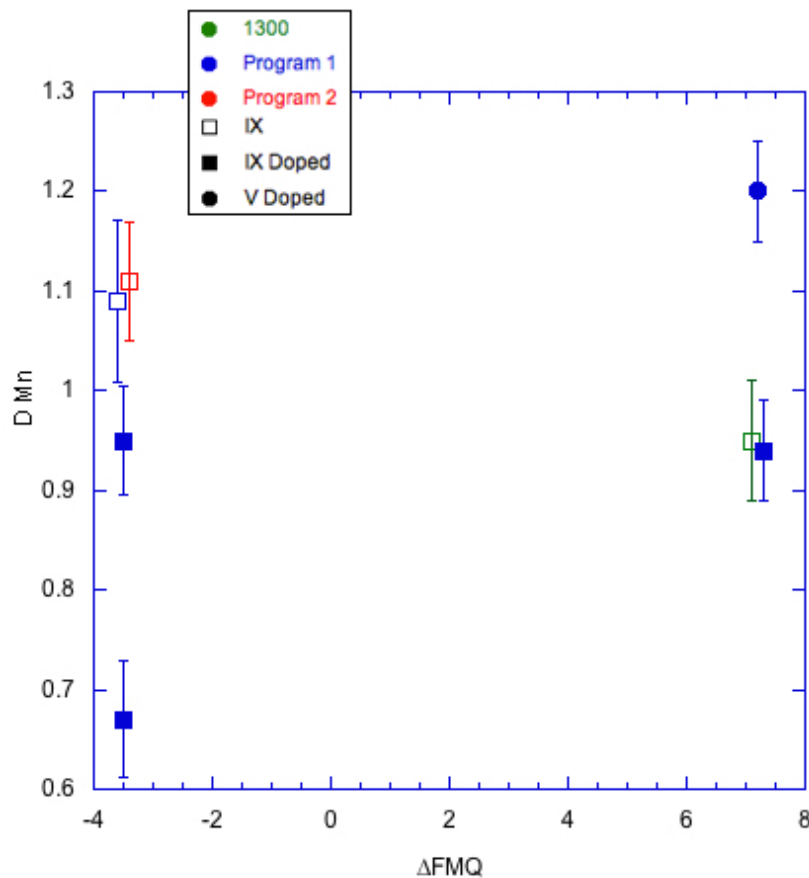

Figure 6: Olivine/glass partition coefficients for Mn plotted against relative oxygen fugacity above and below the FMQ buffer. Error bars are shown and composition and temperature program are represented by shape and color as shown in the legend. IW buffer is at ΔFMQ=-4 and RRO is at ΔFMQ=8 (approximately).

Box 2: Table of experiments run at 1-Atmosphere.

Exp ID	T program	log fO2	duration	composition	phase assemblage	crystal sizes	Notes
SP1	3	IW	46	I DOPED	glass	n/a	
SP2	3	IW	46	V DOPED	ol	5-10 u ol	
SP3	3	IW	46	IX DOPED	ol, spinel, plag	5-20 u plag; 10 u ol	Leaked over top of capsule
SP4	3	O2	47	I DOPED	glass	n/a	Air flow to furnace stopped midway
SP5	3	O2	47	V DOPED	ol	8-15 u ol; 5 u spinel	
SP6	3	O2	47	IX DOPED	ol, spinel	2 u spinel; 5-10 u ol;	
SP7	3	IW	95	V	ol	5-10 u ol	
SP8	3	IW	95	IX	ol, plag	10 u ol; 5-20u plag	
SP9	3	O2	98	V	ol	10-25 u ol	
SP10	3	O2	98	IX	ol, spinel	40 u ol; 5-8 u spinel	
L1	1	IW	22	IX	ol	50 u ol	
L2	1	O2	23	V	glass	n/a	
L3	1	O2	23	IX	ol, spinel	50-100 u ol; 5 u spinel	
L4	2	IW	21	V	glass, ol	a few 30 u hollow ol	Skeletal olivines
L5	2	IW	21	IX	ol, spinel	180 u ol; 5 u spinel	
L6	3	O2	96	V	ol	15 u ol	
L7	3	O2	96	IX	ol, spinel	30 u ol; 5 u spinel	
L8	1	IW	24	IX DOPED	ol, spinel	60 u ol; 5-10 u sp	Fell off loop
L9	1	IW	24	V DOPED	glass	n/a	
L10	1	O2	22	IX DOPED	spinel	2-5 u sp	
L11	1	O2	22	V DOPED	glass	n/a	
L12	1	IW	20	V DOPED	glass	n/a	
L13	1	IW	20	IX DOPED	ol	5-10 u	
L14	1	O2	20	V DOPED	ol	5-10 u	
L15	1	O2	20	IX DOPED	ol, spinel	10 u ol; 5 u spinel	Big quench boundary

NOTE: Experimental ID indicates the sample mechanism used ("SP" prefix is illustrated in Figure 3a and "L" is illustrated at Figure 3b). "T program" refer to the temperature programs described in the methods section. Durations are in hours.

Box 3: Table of piston cylinder experiments run at 1 GPa.

Exp ID	Redox	duration	assembly	Material	NOTES
ApMn1	MW sandwich	96	graphite lined Ni	SD1, H2O, ir	Lost h20; remnant apatites
ApMn2	MW sandwich	96	graphite lined Ni	SD2, H2O, ir	Crystallized melt
ApMn3	RuRuO2 sandwich	96	AgPd lined Ni capsule	SD2, H2O	apatite (10-50 u) and (FeMnTi)O
ApMn4	MW sandwich	96	2-sided graphite lined Pt	SD2, H2O, ir	lost h2o; crystallized other phases
ApMn5	RuRuO2 sandwich	96	Au sandwich buffer	SD2, H2O	Apaties (5 u) glass
ApMn6	graphite	96	Graphite lined Pt no buffer	SD2, H2O, ir	didn't melt
ApMn7	ReReO2 sandwich	96	Au sandwich buffer	SD2, H2O	rhenium phosphate-- no apatite
ApMn8	graphite, pre-reduced	96	Au with added graphite	SD2, H2O, ir	Au melted- eutectic?
ApMn9	graphite	96	Au with added graphite	SD2, H2O, ir	Au melted- eutectic?
ApMn10	Include Si	96	Pt w graphite lining	SD2, H2O, ir, Si	too much si
ApMn11	graphite	96	Pt w graphite lining	SD2, H2O, ir	lots of small crystals
ApMn12	graphite, pre-reduced	96	Pt w graphte lining	SD2, H2O, ir	No crystals
ApMn13	graphite	96	Pt w graphte lining	SD2, H2O, ir	No crystals
ApMn14	Pre-reduced	96	Au	SD2, H2O, ir	No crystals
ApMn15	fused in air	96	Au	SD2, H2O, ir	No crystals
ApMn16	Pre-reduced	96	Au	SD3, H2O, ir	lost h20
ApMn17	fused in air	96	Au	SD3, H2O, ir	apatite 5-15 u; glass matrix
ApMn18	RuRuO2 sandwich	96	Pt sandwich buffer	SD3, H2O	18+19- poison thermocouple
ApMn19	graphite	96	Graphite lined Pt no buffer	SD3, H2O, ir	
ApMn20	RuRuO2 sandwich	96	Pt sandwich buffer	SD3, H2O	20+21- crashed in the middle
ApMn21	graphite	96	Graphite lined Pt no buffer	SD3, H2O, ir	
ApMn22	RuRuO2 sandwich	48	Pt sandwich buffer	SD4, H2O	Apatite 5-10 u throughout
ApMn23	graphite	48	Graphite lined Pt no buffer	SD4, H2O, ir	Apatite 5-10 u
ApMn24	RuRuO2 sandwich	48	Au sandwich buffer	SD4, H2O	Apatite some pluckouts!!
ApMn25	Pre-reduced	48	Au	SD4, H2O, ir	Apatite 5-10 u

NOTE: Durations are presented as hours. The column "Redox" specifies how the redox state was imposed on that experiment. All "Pre-reduced" samples were done so at the IW buffer, as described in the methods section of this report.

grown in these samples. These results show no significant change in the partitioning of manganese into olivine crystals with change in the redox state. The partition coefficient that was recorded to be 0.67 resulted from a sample that showed high variability between measurements. For the other experiments, however, the partition coefficients remain around 1 at both extremes of redox.

Part 2. Apatite-melt partitioning (Piston Cylinder)

Samples 22, 23, 24, and 25 were the most successful runs on the basis of suppression of the growth of accessory phases, quenching to a homogenous glass and growing abundant apatite crystals of sufficient size. These samples were analyzed on the electron probe and the apatite/glass partition coefficients, calculated from these results, are presented in Figure 7. Note the shape of symbols indicating the source of the data as well as the color bar, indicating the temperature at which the experiment was run or alternatively the estimated temperature of apatite crystallization from the Criffell Pluton, as recorded by Miles et al. (2014).

Because of the large partition coefficient from Zone 4 of the Criffell Pluton, plotted on the top left of Figure 7, the y-axis of this graph is a log-10 scale. The size of the error bars relative to the size of the dots would therefore not show on this graph. Error bars are shown in Figure 8 with a broken y-axis. The partition coefficients are all within error of roughly 0.85.

The broken axis in Figure 8 allows a closer look at the partition coefficients calculated for the series of experiments conducted for this study. There is a small decrease in the partition coefficient at fO_2 of ΔFMQ around 8 relative to the experiments run at more reducing conditions. This observation is hardly outside of analytical uncertainty, however.

The large discrepancy in the partition coefficient for the experiments run at reducing conditions (ΔFMQ of approximately 0.5 and -2.5) compared to that calculated from the data for zone 4 of the Criffell Pluton should be noted. There is approximately a 10-fold increase in the D calculated from the results from the empirical study from the results of the experimental study at a similar fO_2.
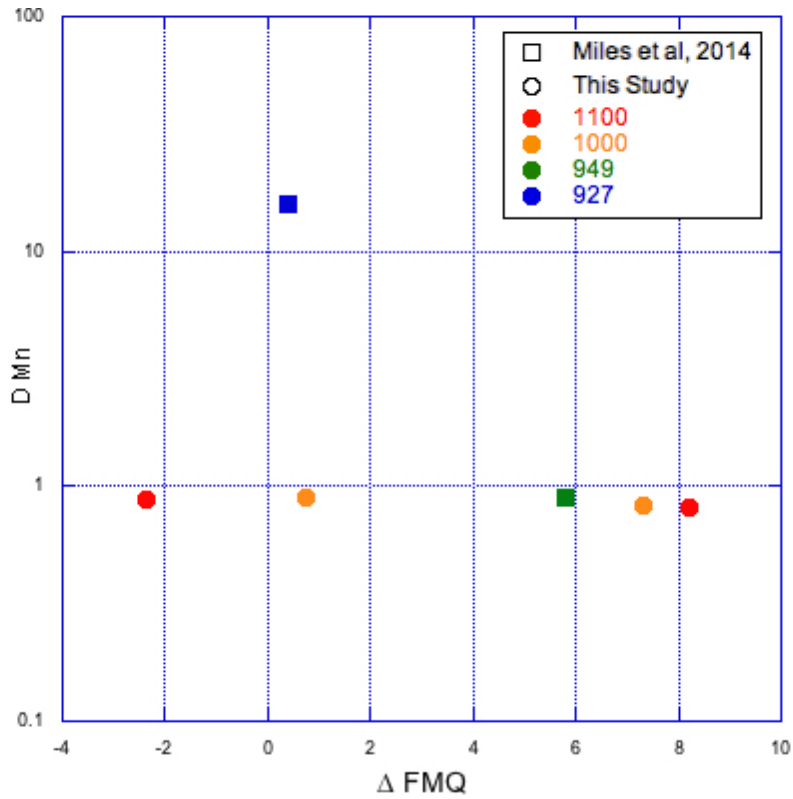
Figure 7: Apatite/Melt partition coefficients for manganese plotted as a function of oxygen fugacity relative to the FMQ buffer. The data is color coded to show temperature, and the shape of the symbol shows the source of the data, from the experiments of this study, or from Miles et al, 2014. Note the IW buffer is around ΔFMQ=-4 and RRO is at ΔFMQ= 8
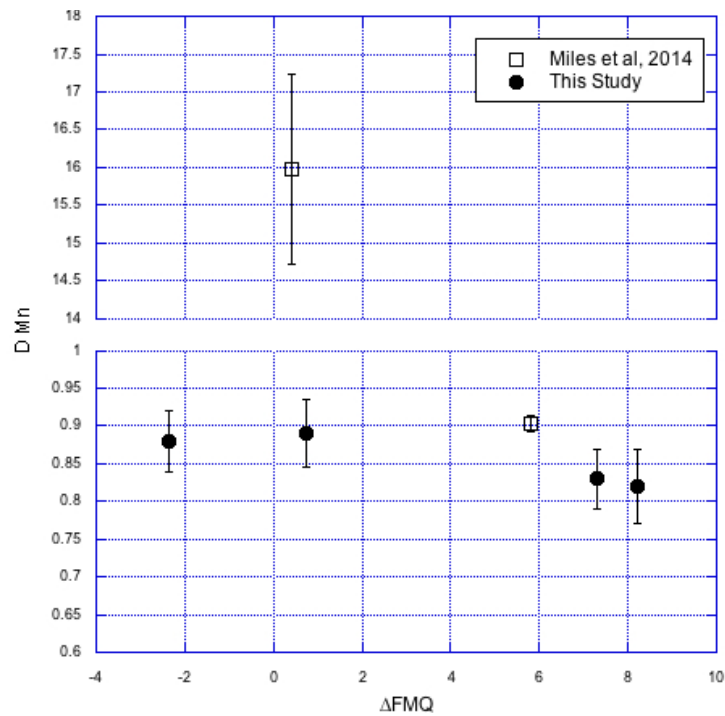

Figure 8: Apatite/melt partition coefficients for Mn again ΔFMQ. Note broken y-axis.

VI. Discussion

Despite the theoretical shift in speciation below ΔFMQ of 6 at 1000°C, there was no associated change in the partitioning of manganese measured across this range of oxygen fugacity. The hypothesized change in speciation was not reflected in the partition coefficients of manganese into olivine crystals at 1-atmosphere or in the partition coefficients of manganese into apatite crystals from experiments in the piston cylinder. The divergence of the experimental results from the theoretical thermochemical speciation of manganese implies that there is no change in speciation across this range of fO_2 in the systems tested.

It is important to consider if the system of each experiment reached equilibrium, as this is important to the validity of results. If the melt has not equilibrated to the imposed redox state, or if the crystals, specifically in regard to apatite, are not primary growth from the equilibrated melt then the results will not be representative of the conditions that imposed on the system. A number of factors indicate that in both sets of experiments the system reached equilibrium.

In the experiments run in the gas-mixing furnaces to measure the partitioning of manganese between olivine crystals and melt, the following evidence for equilibrium exists. For these experiments, the starting composition was a mixture of oxide powders that was fused, quenched and ground to a fine powder. This was done twice to ensure that there were no crystals in the starting material. Additionally, the kinetics of the experiment strongly implies that the melt would have equilibrated to the fO_2 of the surrounding gas mixture. All of the experiments were run at or above the liquidus of the sample and the duration of the run allowed sufficient time for the melt to equilibrate to the surrounding fO_2. This is important because the kinetics of a liquid would allow for equilibration to the imposed redox state much faster than for a solid.

Additionally, the change in redox state was observed visually in the color of each run-product. The samples run at reducing conditions (at IW buffer) had a light pink or mauve color, while the experiments run in pure oxygen, near the RRO buffer had a darker brown color. This noticeable change in color of the same sample composition at different redox condition also implies a change a redox state, as Mn^{2+} is known to have a pink/mauve color. These observations strongly support the assertion that equilibrium was established in the 1-atmosphere experiments.

There are also many lines of evidence suggesting that equilibrium was reached in the piston cylinder experiments. Unlike the 1-atmosphere experiments, the starting material for these experiments was doped with crystals of Durango apatite, a fluoroapatite (FAp) standard. This was done to achieve phosphorus saturation so that apatite would crystallize from the melt. This also introduces the concern that the apatite crystals found in the samples were not grown from the melt, but were rather remnants from the apatite used to dope the sample. The guard against this, the starting composition was fused at 1400℃, quenched, and ground to a glass. This is well above the melting temperature of apatite, so Durango apatite crystals are not expected to remain in the material after this step. Bearing the potential for remnant crystals in mind, however, the following evidence suggests that the apatites grown are primary.
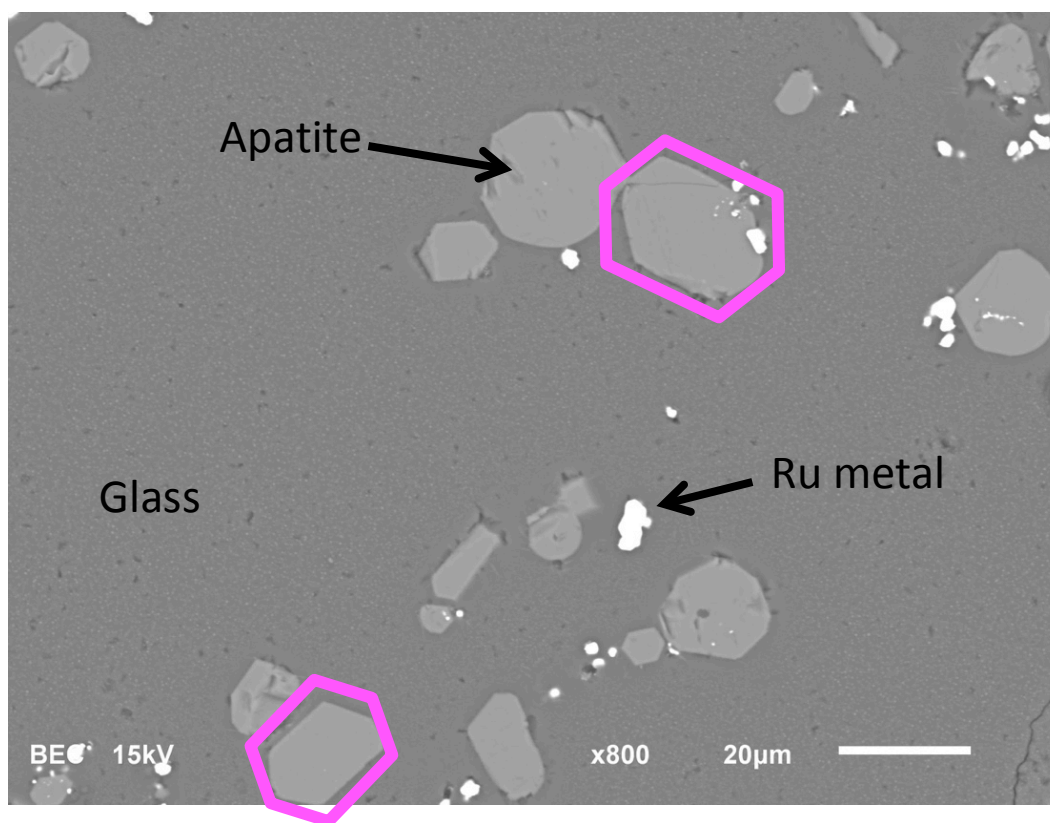

Figure 9: SEM backscattered electron image of sample ApMn22. Note the lack of compositional zoning and the hexagonal crystal habit, outlined in pink.

The apatite crystals reported in this study lacked compositional zoning. This suggests a constant composition throughout the crystal. However, the crystals were not large enough to perform a grain traverse to test this theory. It should be noted that the coloring on an SEM

23

backscattered electron image is shaded to show the average atomic weight of each area. If the crystals were compositionally zoned it would likely correspond to a change in the mean atomic weight, and therefore the color of the zones on the SEM image. Looking at an example image in Figure 9 it is evident that this is not the case.

While the composition across a single crystal cannot be measured, the composition of apatite throughout the sample volume is largely unchanging, suggesting strong phase homogeneity. This can be illustrated by taking a quantitative look at the results from the electron microprobe. The analyses of apatite crystals measured on the electron probe were taken from crystals throughout the sample volume. As presented in Table 3, the standard deviation for the ten analyses of apatite crystals in each sample is less than the error resulting from counting statistics, as reported by the electron probe. The exception to this is sample ApMn24, and this results from a single analysis that has an abnormally high Mn concentration reported.

	Standard deviation	Counting Error
ApMn22	0.027	0.050
ApMn23	0.038	0.050
ApMn24	0.052	0.050
ApMn25	0.027	0.047

Table 3: The standard deviation and error resulting from counting statistics for the compositional data of apatite for each sample

Additionally, the size and growth habit of the apatite crystals in these experiments were also consistent with what would be expected of primary apatite crystallizing from a homogeneous melt. The crystals exhibited the characteristic hexagonal crystal form. This is shown in Figure 9 as well. The procedure used to integrate the doped apatite makes it unlikely that any crystals would remain in the melt, but if they did remain, they would likely be angular fragments of less than 5 microns. This is distinct from the apatite crystals that were observed in the sampled.

	Experiments	Durango
P_2O_5	42.28	40.82
CaO	54.03	53.47
MnO	1.30	0.01
F	0.90	3.53
Cl	0.10	0.39
SrO	0.00	0.06

Table 4: The average weight percent composition of apatite crystals reported in this study, compared to the weight percent composition of the Durango apatite standard

There was a distinct compositional shift in the apatite crystals measured in the samples from this study to that of the Durango apatite starting material. This is demonstrated by the data in Table 4 where the average weight percent composition of apatite crystals reported in this study is presented alongside the composition of the Durango apatite standard. The composition of the standard was calculated by taking the average of three accepted compositions. The first was from the standard composition database used in the probe lab at the University of Toronto in addition to compositions published in the studies by Gardoff, Webster & Harlov (2012) and Roeder et al. (1987). Notably, there is very low fluorine and chlorine concentrations in the apatite from the experiments reported in this study. This likely occurs because the samples were run with excess water and, as such, the anion site would be occupied by a hydroxyl. A large increase in the manganese content of the apatite crystals relative to the standard is also recorded. These observations strongly suggest that the melt was at equilibrium with the oxygen fugacity imposed on it and that the crystals were grown directly from this melt.

The experiments reported in this study found that with an analogous composition and similar temperatures, there is no change in the partitioning of manganese. This suggests that a change in the imposed fO_2 is not the cause of the observed increase in partitioning in zone 4 so other potential causes of this change will be explored. A change in the compatibility of an element in a crystal lattice resulting from a change in speciation is not the only way by which a

large change in partitioning can occur. Another factor controlling partitioning is the activity of a component in a melt and in a crystal lattice. A greater understanding of the relationship between partition coefficient and activity is essential to the explanation of the phenomena recorded in the pluton.

The equation relating the activity of manganese (a_{Mn}) to the molar concentration (X_{Mn}) using an activity coefficient (γ_{Mn}) is presented below. An activity coefficient of 1 (where the activity is equal to the concentration) is applicable to pure substances, but is not applicable to natural systems. Activity coefficients quantify the deviation of the behavior of a substance from ideal behavior. The activity of a species is affected primarily by whole-rock composition and temperature. The relationship between partition coefficient (D) and activity is presented below. This equation states that any parameter that would increase the activity of manganese in apatite (γ_{Mn}^{Ap}) or decrease the activity of manganese in the melt (γ_{Mn}^{melt}) would result in an increase in the partition coefficient, D.

$$a_{Mn} = X_{Mn} \times \gamma_{Mn}$$

$$D = \left(\frac{X_{Mn}^{Ap}}{X_{Mn}^{melt}} \right) \times \left(\frac{\gamma_{Mn}^{Ap}}{\gamma_{Mn}^{melt}} \right)$$

This equation illustrates that the large increase in partition coefficient observed from zone 1 to 4 in the pluton does not necessitate a change in compatibility of manganese and can alternatively be explained as a change in the ratio of activity coefficients. It should be noted that the factors effecting the activity of manganese were not investigated experimentally in this study. Therefore any suggested explanations for the change in partitioning would need experimental study to prove.

One such explanation relates to the change in composition from zones 1 to 4. As shown in Table 5, the composition is changing significantly across these zones. A literature search for compositional affects on the activity of manganese in magmatic systems yielded a few helpful studies. A study by Hirschmann and Ghiorso (1994) investigated the activity of nickel (Ni), cobalt (Co) and manganese in olivine and silicate glass. Figure 10 below is taken from this study. It illustrates that at 950°C there is an increase in roughly 10 wt% SiO_2 (from a komatiitic

composition with 45.77 wt% SiO_2 to an andesitic composition 57.30 wt% SiO_2) associated with a 3-fold increase in the activity coefficient of manganese.
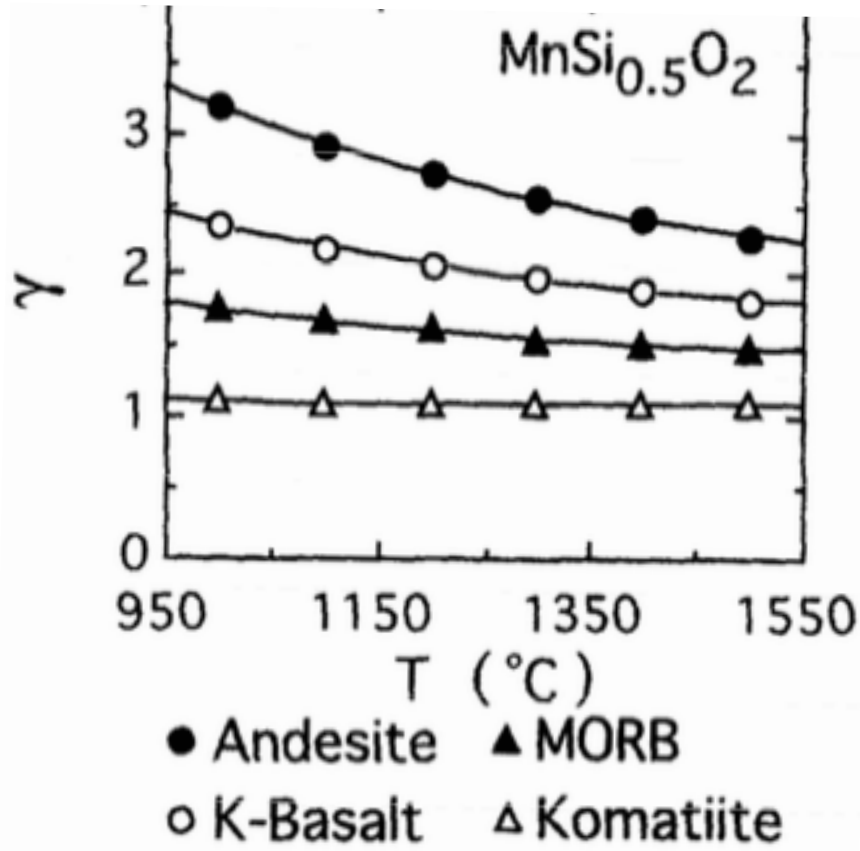

Figure 10: The affect of silica-content on the activity of manganese at variable temperature. The hollow triangles represent a komatiite with 45.77 wt% SiO_2 and the filled circles represent an andesistic composition with 57.30 wt% SiO_2. (Hirschmann and Ghiorso, 1994)

This study by is not directly applicable to what has been presented here as the compositions for the experiments reported in this study are more siliceous, and additionally, the activity of Mn in apatite, a phosphate, is expected to differ from that of Mn in a silicate such as olivine. Nevertheless, the implication that increased SiO_2 in a melt would result in an increase in the activity of manganese parallels observations from the Criffell Pluton. As is shown in Table 5, the concentration of SiO_2 increases from 63.33 wt% in zone 1 to 72.11 wt% in zone 4. The associated increase in partitioning is 10-fold, and implies a 10-fold increase in ratio of the activity coefficients for manganese in apatite and melt. The magnitude of this increase in partitioning suggests that another factor (or other factors) are causing an increase in the activity.

Zone	SiO$_2$	TiO$_2$	Al$_2$O$_3$	Fe Tot	MnO	MgO	CaO	K$_2$O	Na$_2$O	P$_2$O$_5$
1	63.22	0.75	16.09	4.01	0.07	2.85	3.84	3.60	4.30	0.29
2	67.06	0.50	15.93	3.41	0.06	1.83	2.86	4.16	3.90	0.24
3	68.68	0.48	15.76	2.63	0.06	1.56	1.56	4.60	4.04	0.22
4	72.11	0.19	15.04	1.41	0.04	0.77	0.82	4.69	3.97	0.10
ApMn22	58.54	0.61	14.35	3.74	1.50	1.28	4.93	1.67	3.74	1.12
ApMn23	61.46	0.76	15.16	4.40	1.59	1.32	4.67	1.74	4.52	0.85
ApMn24	58.70	0.74	14.41	4.50	1.51	1.25	4.64	1.68	3.82	0.79
ApMn25	59.36	0.58	14.78	3.59	1.52	1.32	4.83	1.66	3.64	1.15

Table 5: Glass compositions for the experiments reported in this study (highlighted blue) and whole rock compositions for the zones of the Criffell Pluton (Miles et al., 2014). A component that has an increase in concentration from zone 1-4 is highlighted in red, and those that decrease are highlighted in orange.

Another possible compositional effect on the partitioning of manganese is a result of the anion in apatite. Figure 11 is an appended version of Table 4 from Pan and Fleet (2002) on the structure and mechanisms of substitution in apatite crystals. According to this study there is a nearly 10-fold increase in the solubility of divalent manganese substituting for calcium is chloro-apatite (ClAp) than in fluoro-apatite (FAp). However, when partition coefficients of each zone of the empirical study were compared to the ratio of chlorine to the sum of chlorine and fluorine $\left(\frac{Cl}{(Cl+F)}\right)$ in each zone, no meaningful correlation was found.

Table 4. Solubility limits of some divalent cations in apatites $Ca_{10-n}M_n(PO_4)_6X_2$.

M	X	n	References
Mn	F	1.37	Ercit et al. (1994)
	Cl	10	Klement & Haselbeck (1965)

Figure 11: An appended version of Table 4 from Pan and Fleet, 2002

Although both of the possible compositional outlined above lack experimental proof they suggest the extent to which both melt and apatite composition can affect the activity of manganese in the system. The whole-rock composition, as shown in Table 5, is very variable from zone 1 to zone 4, as is, to a lesser degree, the apatite composition.

Recent attempts to apply the redox sensor to previously published data from well-characterized samples have yielded geologically unrealistic results (Marks et al., 2016). This comment on Miles et al. (2014) did not find a meaningful correlation between the proposed calibration and the pre-existing measurements of fO_2 from previous studies. This indicates that other factors are likely influencing the manganese content of apatite.

VII. Conclusions

Because natural magmatic systems are so complex, experimental studies are important to our understanding of these systems. In this study, by constraining all variables and testing only a change in redox, the effect of oxygen fugacity on the partitioning of manganese into apatite crystals can be evaluated. This study found that there is no change in the partitioning of manganese into apatite crystals across a range of fO_2 that encompasses the range found on earth. This result suggests that there is no change in the speciation of manganese across this interval of fO_2.

This is supported by the experiments completed at 1-atmosphere and 1300℃. At the RRO buffer at this temperature the theoretical speciation would be approximately 30% trivalent. This is not as significant of a shift in speciation compared to the model at lower temperatures, but it is still a distinct change. This was not recorded in the olivine/melt partition coefficients,

also indicating that the thermochemical speciation model is not reflected in the speciation of manganese in magmatic systems.

The recorded change in partitioning from zone 1 to zone 4 of the Criffell Pluton as reported by Miles et al. (2014), although correlated to a change in redox in these zones, is not caused by a change in speciation. The partitioning of manganese into apatite crystals, therefore, is not a function of oxygen fugacity.

VIII. References

Barin, Ihsan & Platzki, Gregor (1995). *Thermochemical data of pure substances* (3rd ed). VCH, Weinheim ; New York

Carmichael, I. S. (1991). The redox states of basic and silicic magmas: a reflection of their source regions?. *Contributions to Mineralogy and Petrology*,*106*(2), 129-141.

Cottrell, E., Kelley, K. A., Lanzirotti, A., & Fischer, R. A. (2009). High-precision determination of iron oxidation state in silicate glasses using XANES. *Chemical Geology*, *268*(3), 167-179.

Elliott, J. C. (1994). *Structure and chemistry of the apatites and other calcium orthophosphates*. Amsterdam [The Netherlands: Elsevier.

Ghiorso, M. S., & Sack, O. (1991). Fe-Ti oxide geothermometry: thermodynamic formulation and the estimation of intensive variables in silicic magmas. *Contributions to Mineralogy and Petrology*, *108*(4), 485-510.

Goldoff, B., Webster, J. D., & Harlov, D. E. (2012). Characterization of fluor-chlorapatites by electron probe microanalysis with a focus on time-dependent intensity variation of halogens. *American Mineralogist*, *97*(7), 1103-1115.

Hanson, B., & Jones, J. H. (1998). The systematics of Cr3+ and Cr2+ partitioning between olivine and liquid in the presence of spinel. *American Mineralogist*, *83*(7-8), 669-684.

Hirschmann, M. M., & Ghiorso, M. S. (1994). Activities of nickel, cobalt, and manganese silicates in magmatic liquids and applications to olivine/liquid and to silicate/metal partitioning. *Geochimica et Cosmochimica Acta*, *58*(19), 4109-4126.

Holzheid, A. Palme, H., and Chakraborty, S. (1997). The activities of NiO, CoO and FeO in silicate melts. *Chem. Geol*. **139**: 21-38.

Mallmann, G., & O'Neill, H. S. C. (2009). The crystal/melt partitioning of V during mantle melting as a function of oxygen fugacity compared with some other elements (Al, P, Ca, Sc, Ti, Cr, Fe, Ga, Y, Zr and Nb). *Journal of Petrology*, *50*(9), 1765-1794.

Marks, M. A., Scharrer, M., Ladenburger, S., & Markl, G. (2016). Comment on "Apatite: A new redox proxy for silicic magmas?" by Miles AJ, Graham CM, Hawkesworth C., Gillespie MR, Hinton RW, Bromiley GD. *Geochimica et Cosmochimica Acta*.

Miles, A. J., Graham, C. M., Hawkesworth, C. J., Gillespie, M. R., Hinton, R. W., & Bromiley, G. D. (2014). Apatite: A new redox proxy for silicic magmas?.*Geochimica et Cosmochimica Acta*, *132*, 101-119.

Pan, Y., & Fleet, M. E. (2002). Compositions of the apatite-group minerals: substitution mechanisms and controlling factors. *Reviews in Mineralogy and Geochemistry*, *48*(1), 13-49.

Roeder, P. L., MacArthur, D., Ma, X. P., Palmer, G. R., & Mariano, A. N. (1987). Cathodoluminescence and microprobe study of rare-earth elements in apatite. *American Mineralogist*, *72*(7-8), 801-811.

Smythe, D. J., & Brenan, J. M. (2015). Cerium oxidation state in silicate melts: Combined fO 2, temperature and compositional effects. *Geochimica et Cosmochimica Acta*, *170*, 173-187.

Smythe, D. J., Brenan, J. M., Bennett, N. R., Regier, T., & Henderson, G. S. (2013). Quantitative determination of cerium oxidation states in alkali-aluminosilicate glasses using M 4, 5-edge XANES. *Journal of Non-Crystalline Solids*, *378*, 258-264.

Wark D. A. and Watson E. B. (2006) TitaniQ: a titanium-in-quartz geothermometer. Contrib. Mineral. Petrol. 152, 743–754.

Watson, E. B. (1977). Partitioning of manganese between forsterite and silicate liquid. *Geochimica et Cosmochimica Acta*, *41*(9), 1363-1374.

Woodland, A.B. and O'Neill, H.StC. (1997). Thermodynamic data for Fe-bearing phases obtained using noble metal alloys as redox sensors. *Geochim. et Cosmochim. Acta* **61**: 4359-4366.